

Investigation of a hydraulic impact – a technology in rock breaking

Martin Genet*

*Laboratoire de Mécanique et de Technologie,
61 av. du Président Wilson, 94235 Cachan Cedex, France*

Wenyi Yan

*Department of Mechanical and Aerospace Engineering,
Monash University, Clayton VIC800, Australia*

Thanh Tran-Cong

*Computational Engineering and Science Research Centre,
University of Southern Queensland, Toowoomba QLD4350, Australia*

*Corresponding author. Tel: 0033147402225, E-mail: martin.genet@lmt.ens-cachan.fr

Abstract

Finite element method and dimensional analysis have been applied in the present paper to study a hydraulic impact, which is used in a non-explosive rock breaking technology in mining industry. The impact process of a high speed piston on liquid water, previously introduced in a borehole drilled in rock, is numerically simulated. The research is focused on the influence of all the parameters involved in the technology on the largest principal stress magnitude in the rock, which is considered as one of the key factors to break the rock. Our detailed parametric investigation reveals that the variation of the rock material properties, especially its density, has no significant influence on the largest principal stress, which implies a good adaptability of the method for different rock materials. The influences of the depth of the hole and the depth of the water column are also very small. On the other hand, increasing the initial kinetic energy of the piston can dramatically increase the largest principal stress and the best way to increase the initial kinetic energy of the piston is to increase its initial velocity. Results from the current dimensional analysis can be applied to optimize this non-explosive rock breaking technology.

Keywords: *Finite element simulation, Dimensional analysis, Rock breaking, Non-explosive method, Hydraulic impact.*

1. Introduction

Explosives are commonly used to fragment large rock masses in modern mining practice. From the technical point of view, although explosive method is powerful, it does not produce fragments with homogeneous size distribution. In many situations the amount of very fine rocks is high, while in other situations the amount of oversized boulders could be excessive.

Furthermore, explosive method involves complex drilling, blasting, scaling, ground support and the evacuation of people and equipment before blasting. Such a multi-activity cycle is time-consuming, inefficient and unproductively expensive [1]. Another major concern with explosive blasting is the associated danger and undesirable impact on the environment such as fly rocks, air blast, noise pollution and toxic fumes. When blasting occurs close to residential areas, or during tunnel construction, environmental protection regulation could seriously affect the rate of rock excavation. In some cases, blasting would be excluded as an acceptable method of rock breaking. Apart from the breaking of large rock masses for transportability purposes, tunnelling requires more carefully controlled rock breaking. Oversized boulders often cause blockage of mine draw points. When such blockage occurs, extensive shutdown of mine operation will result, causing loss of millions of dollars per hour. Thus, fast, simple, safe and clean methods of breaking boulders are required in some cases to make total mining operation efficient.

To overcome the drawbacks of explosive methods, several non-explosive technologies have been developed in the past [1]. Young [2] provided an overview and compared the pros and cons of various methods of pressurising a borehole in a rock mass, including small charge explosive and propellant, water jets, firing of high speed water slugs, mechanical splitters, and high pressure gases. McCarthy [3] proposed the use of propellant cartridge in a predrilled hole to provide the breaking force. In the latest patent by Young [4], a high-pressure foam was utilized to replace explosive technology. The controlled-foam injection method invented by Young [1, 4] has a number of advantages, including lower maximum pressure and the maintenance of pressure during fracture by virtue of the compressibility of the foam. Another non-explosive rock breaking method was invented and patented by Denisart et al. [5], which is illustrated in Fig. 1. The hydraulic fluid, such as water, is introduced in a pre-drilled

borehole and is impulsively loaded by a high speed piston. The highly pressurized water, with the reflection of the pressure wave, will result in huge stresses in the rock mass, especially at the bottom of the hole, which is a stress raiser. Consequently, cracks will be initiated around the borehole, especially at the bottom, and the pressurized water will penetrate into the cracks, providing the driving force for crack propagation. Eventually, cracks will propagate back to the surface due to free surface effect and a volume of the hard material will be removed.

All the available inventions and patents focused on the principle of the rock breaking methods, i.e., different approaches are used to answer the basic question of how to break a rock mass. In terms of the application of the non-explosive technology, one needs to quantify many parameters, such as the depth of the borehole and the initial velocity of the piston, etc. In the current investigation, the dimensional analysis and numerical method are applied to quantify the hydraulic impact process, which is involved in a non-explosive rock breaking technology as shown in Fig. 1. The efficiency of the impact is evaluated by the largest principal stress magnitude in the rock during an impact process. Numerical results from the investigation will assist industry to quantitatively apply this non-explosive rock breaking technology and, therefore, to improve rock breaking efficiency.

This paper is structured as follows. The finite element model to simulate the hydraulic impact is presented in Section 2. The relationship between the largest principal stress magnitude in the rock and all the processing parameters is discussed in Section 3. In Section 4, detailed numerical results on the influence of all the parameters on the largest principal stress magnitude are discussed. Finally, conclusions are given in Section 5.

2. Impact simulation

The finite element method has been applied to simulate the hydraulic impact process. We use a finite element package, CASTEM, to create the finite element mesh, a PERL script to translate CASTEM meshes into ABAQUS meshes, the commercial package ABAQUS/Explicit to perform the simulations, and a PYTHON script to automate this simulation process.

2.1. Finite element mesh

The borehole, as shown in Fig. 1, can be idealized as a cylinder. Therefore, this problem can be treated as axisymmetric. Moreover, the rock body can be considered as semi-infinite. Infinite elements are used to simulate the semi-infinite body. Figure 2 shows the finite element mesh generated by using CASTEM. The definition of the geometrical parameters shown in Fig. 2 can also be found in Table 1.

As shown in Fig. 2, there is an arc with the radius of R_a at the bottom of the borehole. The reason to introduce the arc is to avoid singularity, which implies an infinite stress. Moreover, it is a good representation of the reality. It is impossible to have a perfect right angle practically when a hole is drilled and a round trace of the tool on the machined part always exists. Further explanation of this assumption can be found in Section 3. Very fine meshes are generated around the corner of the bottom of the hole. Many simulation tests with different mesh densities have been carried out to guarantee that the final mesh used in the calculations is fine enough to obtain convergent numerical results. In the end, there are 122 four-node bilinear elements and 4349 three-node linear elements in the final model.

2.2. Material properties

The piston is normally made of steel, which is assumed to be a homogeneous and isotropic material. We also assume that the piston stays in its elastic domain during the impact process.

Thus we can choose the piston's material data as Young's modulus $E_p = 200 \text{ GPa}$, Poisson's ratio $\nu_p = 0.3$ and density $\rho_p = 7800 \text{ Kg/m}^3$.

As this study does not consider any cracks in the rock, water will be confined within the borehole, and then transfer force and energy from the piston to the rock through deformation and not through flow. In this case, according to Wilson [6], the water can be modelled as an elastic, homogeneous and isotropic solid with these material coefficients: Young's modulus $E_w = 6207813 \text{ Pa}$, Poisson's ratio $\nu_w = 0.4995$, and density $\rho_w = 1000 \text{ Kg/m}^3$. Let's remark

that this material has the key properties for our present study: quasi-incompressibility ($\nu \approx 0.5$) and correct pressure wave speed ($c = \sqrt{\frac{\lambda + 2\mu}{\rho}} \approx 1500 \text{ m/s}$). For further studies,

when cracks will be introduced, an improved model will be used for water.

In the current investigation, the rock in this simulation is simplified as an elastic, homogeneous and isotropic solid. In reality, rock, as a natural material, consists of crystal, grains, cementitious materials, voids, pores and flaws, see [7]. However, at the first stage of investigating this non-explosive rock breaking technology, our current objective is to understand and quantify the impact process. Considering the influence of the inhomogeneous microstructure of rock material will be our next task. On the other hand, because of the uncertainty of the microstructure and its inhomogeneity, the assumed isotropic rock in our model can be treated as a representative of the real material and the results from this assumption will still be practically useful, especially for companies which intend to develop

relevant universe equipments for this non-explosive technology. Furthermore, the possible plastic deformation of the rock is not taken into account in the present research, neither the creation nor the propagation of cracks, which will be our future study. Consequently, there are three parameters to describe the rock: Young's modulus E_r , Poisson's ratio ν_r , and its density ρ_r .

2.3. Contact simulation

As shown in Fig. 1 and Fig. 2(a), there are three pairs of contacts involved in the impact process, i.e., the contact between the piston and the water, the contact between the piston and the rock, and the contact between the water and the rock. We use the hard contact algorithm from ABAQUS without damping to simulate these contacts. The friction is also neglected in our simulation. Practically, the friction between water and piston or rock should be very low. Further study will be carried out after we obtain reliable friction value involved in the contact between piston and rock.

2.5. Simulation

The only initial condition in this problem is the initial velocity of the piston, which is an additional parameter of the problem. All the impact simulations were carried out by using ABAQUS/Explicit. The effect of the hydraulic impact is evaluated by the maximum principal stress in the rock. As an example of our finite element simulation results, Fig. 3 shows the distribution of the maximum principal stress magnitude in the structure at the instant when the shockwave arrives at the bottom of the hole. It clearly indicates that the largest maximum principal stress, the largest principal stress in short, occurs at the bottom of the hole. Irrespective of microstructures, cracks will possibly initiate at this position with this largest stress magnitude in the rock. Figure 4 shows the corresponding direction field of the

maximum principal stress at this local area in the rock. One can imagine, once cracks initiate, the highly pressurized water will penetrate into the cracks and drive the cracks to propagate, which will be the core of the investigation to understand the rock breaking in our future study.

3. Dimensional analysis

All the parameters involved in the simulation are listed in Table 1. Here, the radius of the piston is the same as the radius of the borehole. Dimensional analysis is a powerful method to systematically carry out parametrical study on a complicated problem involving many parameters, see examples [8-10]. This method is applied in the current investigation. The objective variable in our dimensional analysis is chosen as the largest principal stress in the rock, σ_m , during an impact process. The rock material can be roughly considered as brittle material. According to Coulomb's criterion of maximum normal stress, the maximum principal stress will initiate cracks in the rock and lead to the fragmentation of rock mass. Generally, the largest principal stress is a function of all the parameters listed in Table 1, i.e.,

$$\sigma_m = f(L_p, E_p, \nu_p, \rho_p, V_p, D_w, E_w, \nu_w, \rho_w, R_h, D_h, R_a, E_r, \nu_r, \rho_r). \quad (1)$$

According to the Buckingham Π -theorem [11] for dimensional analysis, the number of parameters can be reduced based on the number of fundamental dimensions presented in the physical problem by using dimensionless parameters. For this purpose, D_h , the depth of the hole, ρ_p , the density of the piston and E_p , the Young modulus of the piston are chosen as the primary quantities that express all the fundamental dimensions of the physical problem (m, N, s). Therefore, the dimensionless function for the largest principal stress is

$$\frac{\sigma_m}{E_p} = \Pi_1 \left(\frac{L_p}{D_h}, \nu_p, \frac{V_p}{E_p^{1/2} \times \rho_p^{-1/2}}, \frac{D_w}{D_h}, \frac{E_w}{E_p}, \nu_w, \frac{\rho_w}{\rho_p}, \frac{R_h}{D_h}, \frac{R_a}{D_h}, \frac{E_r}{E_p}, \nu_r, \frac{\rho_r}{\rho_p} \right). \quad (2)$$

Among all the dimensionless parameters in Eq. (2), some values can be considered as unchanged in this physical problem. The piston is generally made from steel and water is normally used as the liquid in this technology. Therefore, the material data for the piston and the water can be treated as constant. Consequently, the following dimensionless parameters will be considered constant in our model:

$$\nu_p = 0.3, \quad \nu_w = 0.4995, \quad (3)$$

$$\frac{E_w}{E_p} = \frac{6207813}{2 \times 10^{11}} = 31 \times 10^6, \quad \frac{\rho_w}{\rho_p} = \frac{1000}{7800} = 0.128. \quad (4)$$

Therefore, the dimensionless function (2) can be simplified as

$$\frac{\sigma_m}{E_p} = \Pi_2 \left(\frac{L_p}{D_h}, \frac{V_p}{E_p^{1/2} \times \rho_p^{-1/2}}, \frac{D_w}{D_h}, \frac{R_h}{D_h}, \frac{R_a}{D_h}, \frac{E_r}{E_p}, \nu_r, \frac{\rho_r}{\rho_p} \right). \quad (5)$$

After this dimensional analysis, the number of variables involved in the stress analysis has reduced from 15 in the original Eq. (1) to 8 in Eq. (5).

Based on the understanding of this physical problem, the following limits of the domains for geometrical parameters are appropriated for this problem:

$$\frac{L_p}{D_h} \in [0.1; 0.8], \quad \frac{D_w}{D_h} \in [0.1; 0.8]. \quad (6)$$

$$\frac{R_h}{D_h} \in [0.01; 0.5], \quad \frac{R_a}{D_h} \in [0.001; 0.05]. \quad (7)$$

Referring to [12], the domains of the mechanical properties of different types of rocks are shown in Table 2. According to this table, after choosing $E_p = 200 \text{ GPa}$ and $\rho_p = 7800 \text{ Kg/m}^3$, one can define the domains for dimensionless variables linked to the rock material as follows:

$$\frac{E_r}{E_p} \in [0.05; 0.5], \quad \nu_r \in [0.1; 0.35], \quad \frac{\rho_r}{\rho_p} \in [0.25; 0.4]. \quad (8)$$

According to Denisart et al. [5], the initial velocity of the piston can vary from 10 *m/s* to 200 *m/s*, which corresponds to the following domain of the dimensionless initial velocity:

$$\frac{V_p}{E_p^{1/2} \times \rho_p^{-1/2}} \in [0.0020; 0.0395]. \quad (9)$$

In our numerical simulations, the limits of some parameters domains have been adjusted due to numerical instability problem. The Poisson's ratio of water is 0.4995, which is close to the value of 0.5 of incompressible materials. Additionally, the water is highly confined in the borehole and exposed to a highly compressive load from the impact of the high speed piston. Due to these factors, the calculation can sometimes lead to numerical instability [13]. A unsuccessful numerical instability calculation can be detected by observing large abnormally distorted and penetrated deformed meshes. To overcome this instability problem, some values lower than the upper limit or higher than the lower limit of the domains defined in above Eqs (6-9) were chosen sometimes. In the following section, only the correct results from the stable calculations are reported. It is believed that the fitted laws in the restricted domains of study in the following section are valid in the entire domains defined in Eqs (6-9).

4. Results and discussions

4.1. Influence of rock properties

4.1.1. Rock density

The effect of rock density is considered first. Figure 5 shows the influence of the normalized rock density, ρ_r / ρ_p , on the normalized largest principal stress in the rock during the impact process, σ_m / E_p .

We have considered the two limit values of the domains of all the dimensionless parameters in Eq. (5), one by one from Fig. 5(a) to Fig. 5(g), while fixing the values of all the others dimensionless parameters at the middle values of their domains, which are defined in Eqs (6-9). For example, the two curves in Fig. 5(a) are obtained for $L_p/D_h = 0.17$ and $L_p/D_h = 0.58$ respectively while fixing $\nu_r = 0.19$, $E_r/E_p = 0.3$, $R_a/D_h = 0.026$, $R_h/D_h = 0.26$, $D_w/D_h = 0.5$ and $V_p/(\rho_p^{-1/2}E_p^{1/2}) = 0.013$.

Figures 5(a-g) clearly indicate that the variation of the normalized largest principal stress σ_m/E_p due to the change of the normalized rock density ρ_r/ρ_p from 0.25 to 0.4 in all the studied cases is negligibly small. Because all the studied cases have covered the domains of this physical problem, one can deduce that it is generally correct that the influence of the variation of rock density on the largest principal stress in the rock can be neglected. Consequently, the dimensionless rock density in Eq. (5) can be removed and the dimensionless stress function can be further simplified as

$$\frac{\sigma_m}{E_p} = \Pi_3 \left(\frac{L_p}{D_h}, \frac{V_p}{E_p^{1/2} \times \rho_p^{-1/2}}, \frac{D_w}{D_h}, \frac{R_h}{D_h}, \frac{R_a}{D_h}, \frac{E_r}{E_p}, \nu_r \right). \quad (10)$$

4.1.2. Rock Poisson's ratio

Figure 6 shows the numerical results of the normalized largest principal stress in the rock during the impact for different values of the Poisson's ratio of the rock. All the others dimensionless parameters in Eq. (10) are fixed at their middle values of their domains, and only the Poisson's ratio of the rock changes from one calculation to another. As shown in Fig. 6, the normalized largest principal stress increases slightly with the increasing of the Poisson's ratio of the rock. The set of the numerical data can be well fitted by the following exponential function:

$$\frac{\sigma_m}{E_p} = 0.0043 + 0.0107 \times V_r^{2.98} . \quad (11)$$

4.1.3. Rock Young's modulus

Figure 7 shows the variation of the normalized largest principal stress in the rock during the impact for different normalized values of the Young's modulus of the rock. Similar to Fig. 6, σ_m / E_p increases slightly with the increasing of E_r / E_p from 0.1 to 0.5. The set of the numerical data is also fitted by an exponential function, which is shown with the thick curve in Fig. 7.

4.2. Influence of borehole dimensions

4.2.1. Borehole depth

The depth of the borehole, D_h , is chosen as the primary length in the dimensional analysis. Its influence on the problem can be implicitly reflected in the parametric study of other dimensionless length parameters, such as the dimensionless piston length and the dimensionless water depth. But it is understandable that the depth of the borehole has no direct influence on the largest principal stress in the rock, and that is the reason to choose it as the primary length to normalize the other parameters.

4.2.2. Borehole radius

Figure 8 shows the influence of the normalized borehole radius R_h / D_p on the normalized largest principal stress in the rock σ_m / E_p while other parameters are fixed at the middle values of their domains. It indicates that σ_m / E_p increases gradually with R_h / D_p . Bear in mind, the borehole radius is equal to the radius of the water column and the radius of the

piston. Increasing borehole radius means increasing the radius of the piston, and therefore, increasing the initial kinetic energy of the piston with fixed initial velocity. This influence in real value is very significant.

It is interesting to plot the instantaneous average velocity and the instantaneous kinetic energy of the piston over the impacting time for several values of the dimensionless radius of the hole. Figures 9 and 10 show these results. In Fig. 9, at the beginning, the piston is moving down, that is why the average velocity is negative. Then its average velocity decreases, and at

$\frac{t}{D_h} \times \rho_p^{1/2} \times E_p^{-1/2} = 7$, the piston has zero averaged velocity. After that, the piston is coming

up, so its average velocity is increasing. This point can also be followed in Fig. 10: the piston

starts with its kinetic energy, which decreases until $\frac{t}{D_h} \times \rho_p^{1/2} \times E_p^{-1/2} = 7$ where it is null,

and then increases because the piston is coming up. Additionally, from Fig. 9, the average

velocity of the piston does not depend on the borehole radius, and from Fig. 10, the kinetic

energy of the piston depends on the radius of the hole, which is obvious because the radius of

the hole is also the radius of the piston and the initial kinetic energy strongly depends on the

radius of the piston. However, its evolution is quite similar from one value to another, which

is obviously linked to the fact that the average velocity is the same for all curves in Fig. 9.

This can be explained by the fact that both the kinetic energy of the piston and the energy that

is transmitted to the water depend on the radius of the piston in the same way: they both are

proportional to the cross section area of the piston, i.e., the square of its radius. Then, if the

piston has a larger radius, it will have more initial kinetic energy, but it will also transmit

more energy to the water, so its kinetic energy will decrease faster. This remark is important,

and as discussed below, the kinetic energy of the piston is a key factor to determine the largest

principal stress in the rock.

To understand this, an impact process is discussed by following Fig. 11, which shows the maximum principal stress in the element that has the largest principal stress and the instantaneous average velocity of the piston versus impacting time for $R_h/D_h = 0.0167$:

- The piston hits the water with its initial velocity at the beginning of the simulation, which starts the impact process.

- The created shockwave comes down in the water, and arrives at the bottom of the borehole at $t/D_h \times \rho_p^{1/2} \times E_p^{-1/2} = 2$. Here is the first peak in the stress curve, with $\sigma/E_p = 1 \times 10^{-3}$.

- Then the shockwave climb back to the surface (the material behaviour of the water is very different from the others material behaviours, so the transmission of energy is low) and the stress at the bottom of the hole reduces because of the dispersion of energy.

- When the shockwave arrives at the surface at $t/D_h \times \rho_p^{1/2} \times E_p^{-1/2} = 4$, it is reflected and comes down again, but with more energy because the piston is still coming down.

- Thus, the second peak in the stress curve will be greater, with $\sigma/E_p = 1.7 \times 10^{-3}$ at $t/D_h \times \rho_p^{1/2} \times E_p^{-1/2} = 6$.

- And when the shockwave climbs back and arrives at the surface for the second time, at $t/D_h \times \rho_p^{1/2} \times E_p^{-1/2} = 8$, the piston has no more velocity downward and is going up.

- So the shockwave comes down again with less energy, and the third peak in the stress curve will be smaller, with $\sigma/E_p = 1.6 \times 10^{-3}$ at $t/D_h \times \rho_p^{1/2} \times E_p^{-1/2} = 10$.

It can be conclude that the largest principal stress appears in the rock when the shockwave arrives at the bottom of the hole the last time while the piston still having some velocity

downward. It indicates that the kinetic energy of the piston plays an important role in the determination of the largest principal stress.

4.2.3. Arc radius at borehole bottom

This parameter, the arc radius at the borehole bottom, as shown in Fig. 2, is introduced to avoid the problem of infinite stress at the corner and allow a better modelling of the geometry of the hole in a real situation. Obviously, it will have a substantial influence on the stress in the rock. Figure 12 shows its influence on the problem. The thick curve in Fig. 12 represents an exponential function to fit the numerical dots. The stress tends to infinity when the radius of the arc closes to zero, which is expected because of the problem of singularity when $R_a = 0 \text{ mm}$. Practically, this parameter will never be equal to zero, and its value can be estimated from the documentation of the active part of the tool used to drill the hole, in addition to the consideration of the rock material, or from experimental tests.

4.2.4. Water depth

Figure 13 shows the influence of D_w on the largest principal stress in the rock and on the time to reach this value, when all the other dimensionless parameters are fixed at the middle values of their domains. The largest principal stress decreases and that the time to reach that stress increases when the depth of water increases, as seen in Fig. 13. This conclusion can be explained by the fact that the deeper the water is, the more the energy can disperse from the water to the rock, and therefore, it results to a smaller largest principal stress in the rock at the bottom of the hole. This relationship depends on the distance travelled by the shockwave, and Fig. 13 indicates that the normalized stress curve consists of two linear parts with the corner at $D_w/D_h = 0.35$. Furthermore, the slope of the normalized stress curve depends on the number of return trips that the shockwave has made before the largest principal stress is

reached and the change of the curve's slope is linked to the discontinuity of the curve for the time to reach the largest stress, and is explained in detail below.

The variation of the time to reach the maximum principal stress with the change of the water depth, shown in Figure 13, is due to the combination of two facts:

- when the depth of water increases, the time for the shockwave to travel from the surface of the water to the bottom of the hole increases too, so the time to reach the largest principal stress increases.

- and when the water becomes deep enough, the largest principal stress is not reached at the third time when the shockwave arrives at the bottom of the hole, but the second time. This can be followed in Fig. 14(a) and 14(b), which give the maximum principal stress in the element that has the largest principal stress in the rock and the kinetic energy of the piston versus times, respectively for $D_w/D_h = 0.333$ and $D_w/D_h = 0.417$, which are respectively around the corner of the stress curve and the dropping part of the time curve in Fig. 13. Figure 14(a) shows that the largest principal stress is reached at the third time when the shockwave arrives at the bottom of the hole for $D_w/D_h = 0.333$ and Fig. 14(b) shows it is reached at the second time for $D_w/D_h = 0.417$. This is the reason for the time dropping between $D_w/D_h = 0.333$ and $D_w/D_h = 0.417$ and the appearance of the corner of the stress curve in Fig. 13.

Figure 13 indicates that reducing the water depth can increase the largest principal stress in the rock. In terms of the entire rock breaking technology, pressurized water is needed to drive crack propagation once cracks are initiated in the rock. Therefore, it is not recommended to increase the largest principal stress in the rock by reducing the water depth.

4.3. Influence of piston dimensions

The radius of the piston is the same as R_h , the radius of the hole. Its influence has been studied in the previous subsection.

4.3.1. Piston length

Figure 15 shows that the normalized largest principal stress increases continuously with the increasing of the normalized piston length. The longer the piston is, the higher its initial energy is because of the fixed initial velocity. Therefore, the stress in the rock increases. Such an influence is significant. Figure 15 also shows that the time to reach the largest principal stress magnitude has an irregular relationship with the piston length. This can be explained by Fig. 16(a-c), which show the relationships between the normalized maximum principal stress in the element that has the largest value in the rock during the impact, the normalized kinetic energy of the piston and the normalized impacting time for different values of the normalized piston length, $L_p/D_h = 0.1667$ in Fig. 16(a), $L_p/D_h = 0.4167$ in Fig. 16(b), and $L_p/D_h = 0.5833$ in Fig. 16(c), while the other dimensionless parameters are fixed at the middle values of their domains. Figure 16(a) indicates that when the shockwave climbs back to the surface at the second time when the slope of the curve of the kinetic energy changes, at

$t/D_h \times \rho_p^{1/2} \times E_p^{-1/2} = 7.5$, the piston has no more velocity downward and is coming up (its

kinetic energy has already been null), which means that all its energy has already been transferred to the structure, so the largest principal stress has already been reached, the second time when the shockwave arrives at the bottom of the hole ($\sigma_m/E_p = 3.5 \times 10^{-3}$ at

$t/D_h \times \rho_p^{1/2} \times E_p^{-1/2} = 6$). It is exactly the same process as in previous Subsection 4.2.2. In the

Fig. 16(b), the impacting process is similar: the largest principal stress is also reached at the

second time when the shockwave arrives at the bottom of the hole, at $t/D_h \times \rho_p^{1/2} \times E_p^{-1/2} = 6$, but due to the higher impacting energy, the value of the normalized largest principal stress is larger, with $\sigma_m/E_p = 4.5 \times 10^{-3}$. And Fig. 16(c) is for an even longer piston: the piston still have some downward velocity (its kinetic energy has not been null) when the shockwave returns at the surface for the second time at $t/D_h \times \rho_p^{1/2} \times E_p^{-1/2} = 7.5$. Therefore, the largest principal stress is reached at the third time when the shockwave arrives at the bottom of the hole: $\sigma_m/E_p = 5.3 \times 10^{-3}$ at $t/D_h \times \rho_p^{1/2} \times E_p^{-1/2} = 10$. This is the reason why the time to reach the largest principal stress is irregular as shown in Fig. 15.

4.3.2. Piston's initial velocity

Figure 17 shows the variation of the normalized principal stress in the rock with the change of the normalized initial velocity of the piston. It clearly indicates that the normalized largest principal stress increases linearly with the normalized velocity and the variation rate is significant.

4.3.3. Initial kinetic energy of the piston

The influence of the dimensions of the piston and its initial velocity on the largest principal stress in the rock have been investigated. We will now try to understand the global influence of its initial kinetic energy, which embrace all these parameters:

$$K_p = \frac{1}{2} \times \rho_p \times \pi \times R_p^2 \times L_p \times V_p^2. \quad (12)$$

Figure 18 shows the evolution of the normalized largest principal stress in the rock during the impact with respect to the normalized initial kinetic energy of the piston. The initial kinetic energy is changed by three approaches separately, i.e., changing the piston length, changing

the piston radius and changing the initial velocity of the piston, while keeping the other parameters fixed at the middle values of their domains. Numerical results from the three approaches are depicted by three curves in Fig. 18. All these curves indicate that increasing the initial kinetic energy can increase the largest principal stress in the rock. For the purpose of increasing the largest principal stress in the rock over 800 MPa for $E_p = 200 \text{ GPa}$ through increasing the initial kinetic energy, Fig. 18 indicates that the most effective way is to increase the piston's initial velocity.

5. Conclusions

The hydraulic impact problem of a non-explosive rock breaking technology has been studied. Dimensional analysis and finite element method have been applied to systematically investigate the influence of all the parameters involved in the impact process, which includes the geometrical parameters and the properties of rock, piston and water. Major conclusions from our investigation are summarized below:

- The influences of rock's material properties on the largest principal stress in the rock are small, which implies a good adaptability of the method for different rock materials.
- The shape of the bottom of the hole has a significant impact on the problem.
- The largest principal stress in the rock decreases if the depth of water is increased.
- Increasing the initial kinetic energy of the piston has a significant influence on the problem: it implies an increase of the largest principal stress in the rock and a variation of the time to reach that value.
- The best way to increase the largest principal stress in the rock by increasing the initial kinetic energy of the piston is to increase its initial velocity.

Acknowledgement

This work has been partially supported by the Australia Research Council through the grant ARC-LP0562720. The authors also want to acknowledge Laurent Champaney for his useful Perl scripts.

References

1. **Singh S.P.** Non-explosive applications of the PCF concept for underground excavation. *Tunnelling and Underground Space Technology* 13 (1998) 305-311.
2. **Young C.** Controlled foam injection for hard rock excavation. In 37th U.S. Rock Mechanics Symposium (1999), Vail, Colorado.
3. **McCarthy D.E.** Method apparatus and cartridge for non-explosive rock fragmentation. U.S. Patent (1998) No. 5803551.
4. **Young C.** Controlled foam injection method and means for fragmentation of hard compact rock and concrete. U.S. Patent (2002) No. 6375271.
5. **Denisart J.P., Edney B.E., Lemcke B.** Method of breaking a hard compact material, means for carrying out the method and application of the method. U.S. Patent (1976) No. 3988037.
6. **Wilson E.L.** Three-dimensional static and dynamic analysis of structures. 3rd Edition. Berkeley: Computers and Structures, Inc. 2002.
7. **Jaeger J.C., Cook N.G.W.** Fundamentals of rock mechanics. 3rd Edition. London: Chapman and Hall, 1979.
8. **Anderson T.L.** Fracture mechanics: Fundamentals and applications. 2nd Edition. Boca Raton: CRC Press, 1995.

9. **Tunvisut K., O'Dowd N.P., Busso E.P.** Use of scaling functions to determine mechanical properties of thin coatings from microindentation tests. *International Journal of Solids and Structures* 38 (2001) 335-351.
10. **Yan W., Sun Q., Feng X.-Q., Qian L.** Analysis of Spherical Indentation of Superelastic Shape Memory Alloys. *International Journal of Solids and Structures* 44 (2007) 1-17.
11. **Buckingham, E.** On Physically Similar Systems; Illustrations of the Use of Dimensional Equations. *Physical Review* 4 (1914) 345-376.
12. **Russell Mineral Equipment Pty. Ltd.** Internal Report. 2003.
13. **ABAQUS v. 6.4.** Analysis/Theory Manuals. 2003.

Table 1. List of all the parameters involved in the impact simulation

Piston	Water	Rock	Borehole
E_p : Young's modulus	E_w : Young's modulus	E_r : Young's modulus	R_h : radius
ν_p : Poisson's ratio	ν_w : Poisson's ratio	ν_r : Poisson's ratio	D_h : depth
ρ_p : density	ρ_w : density	ρ_r : density	R_a : arc radius
L_p : length	D_w : depth		
V_p : initial velocity			

Table 2. Mechanical properties of typical rock materials

Rock material	Density (Kg / m ³)	Young modulus (GPa)	Poisson's ratio
Granite	2500 - 2800	35 - 80	0.1 - 0.2
Basalt	2400 - 2900	20 - 100	0.1 - 0.3
Sandstone	2200 - 2700	10 - 40	0.2 - 0.3
Dolerite	2900 - 3100	40 - 90	0.1 - 0.3
Limestone	2000 - 2800	10 - 50	0.2 - 0.35
Andesine	2500 - 2800	30 - 60	0.1 - 0.25

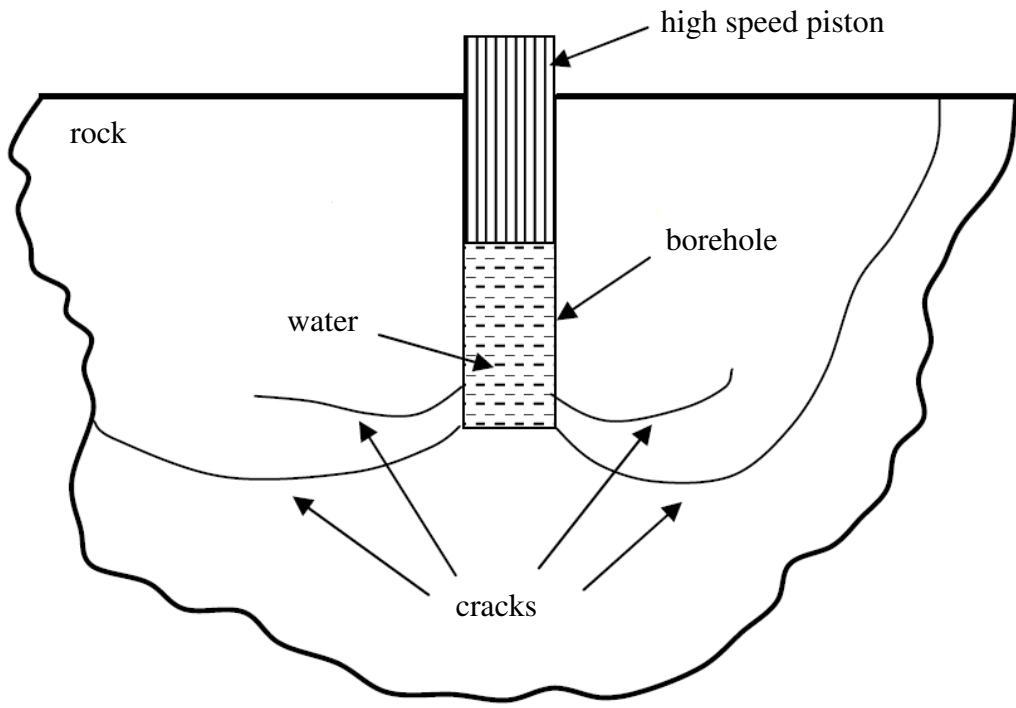


Fig. 1. Illustration of the hydraulic rock breaking technology.

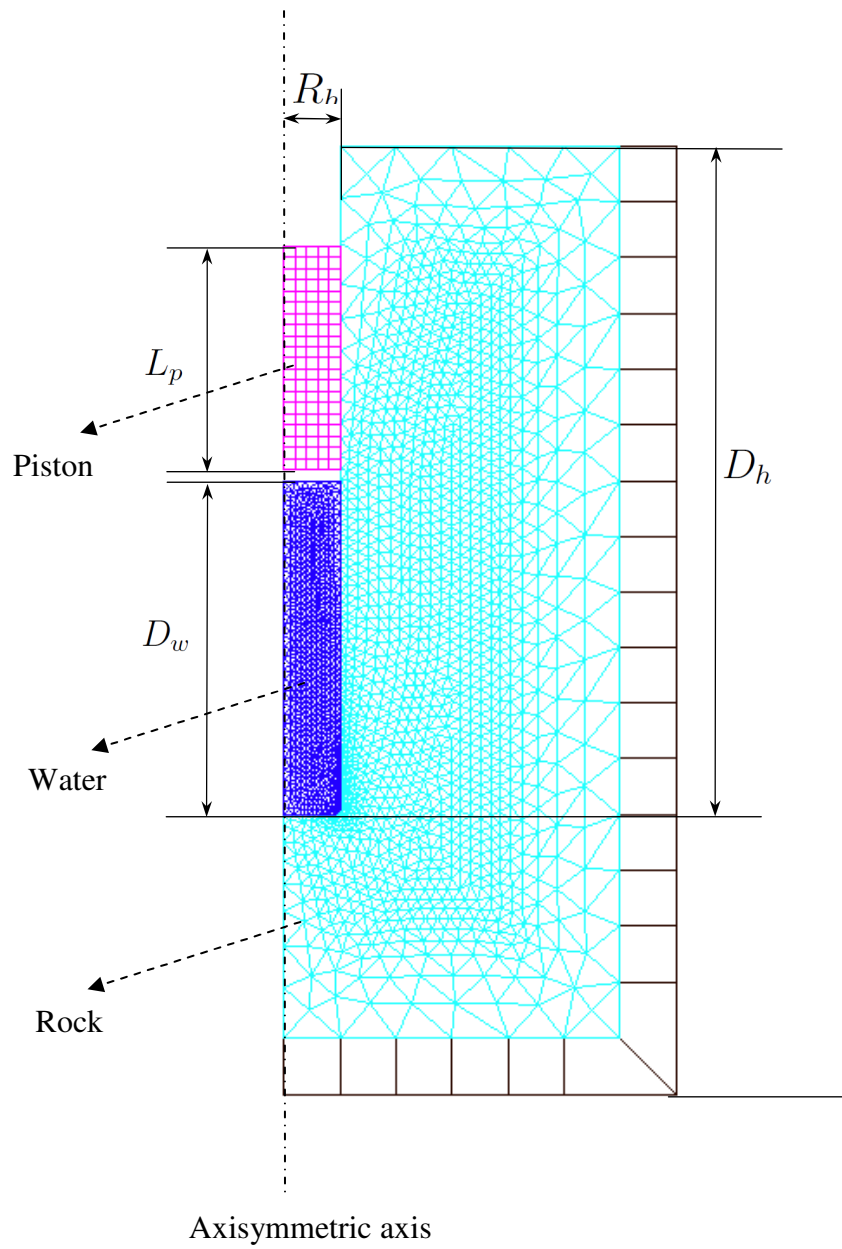


Fig. 2(a)

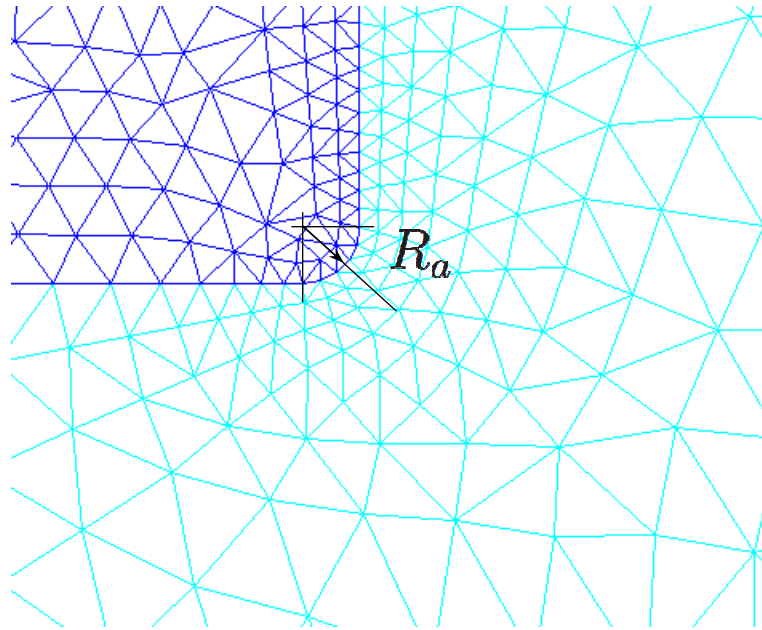


Fig. 2(b)

Fig. 2. Finite element mesh and relevant geometrical parameters: (a) global mesh; (b) local mesh around the bottom of the borehole.

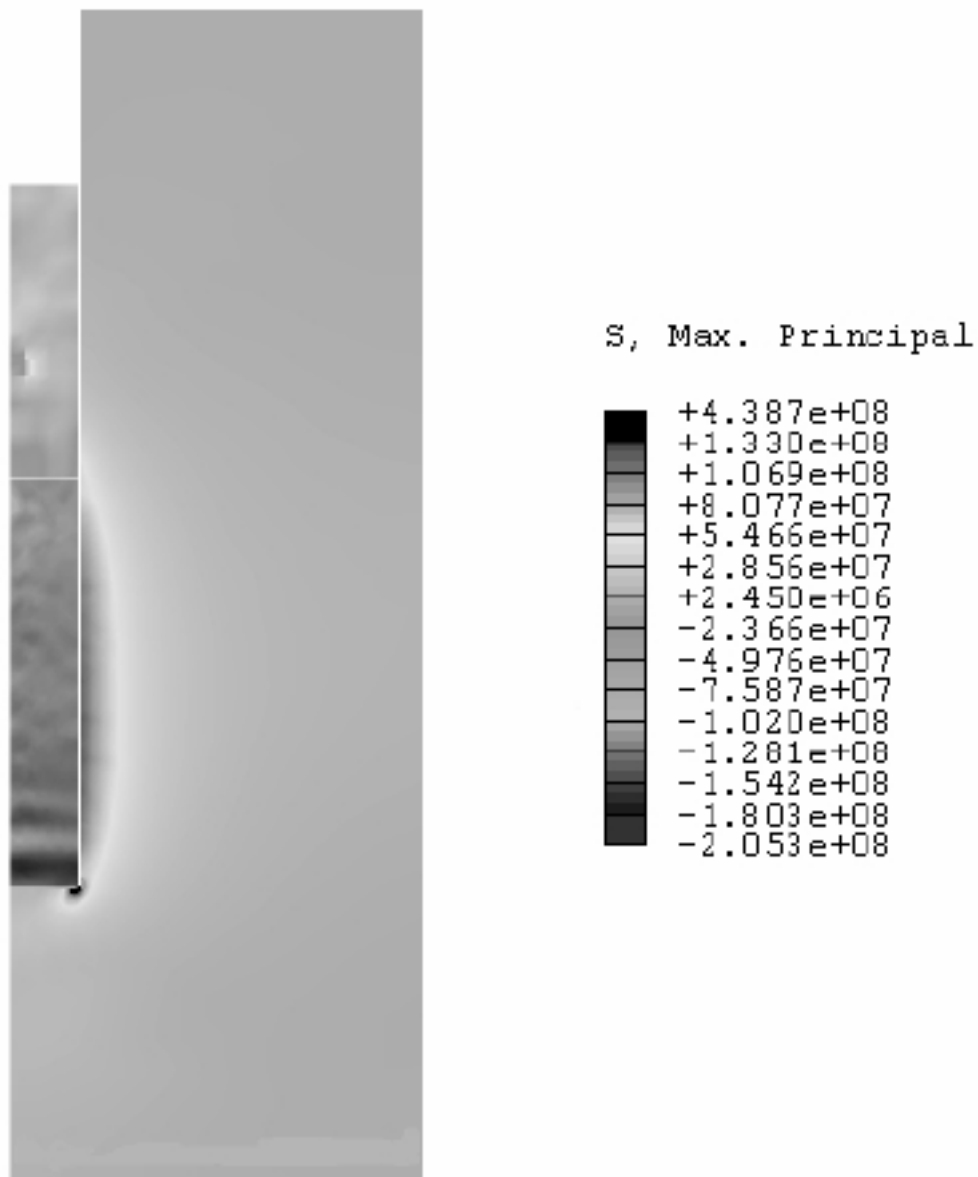


Fig. 3. Maximum principal stress field, in the structure.

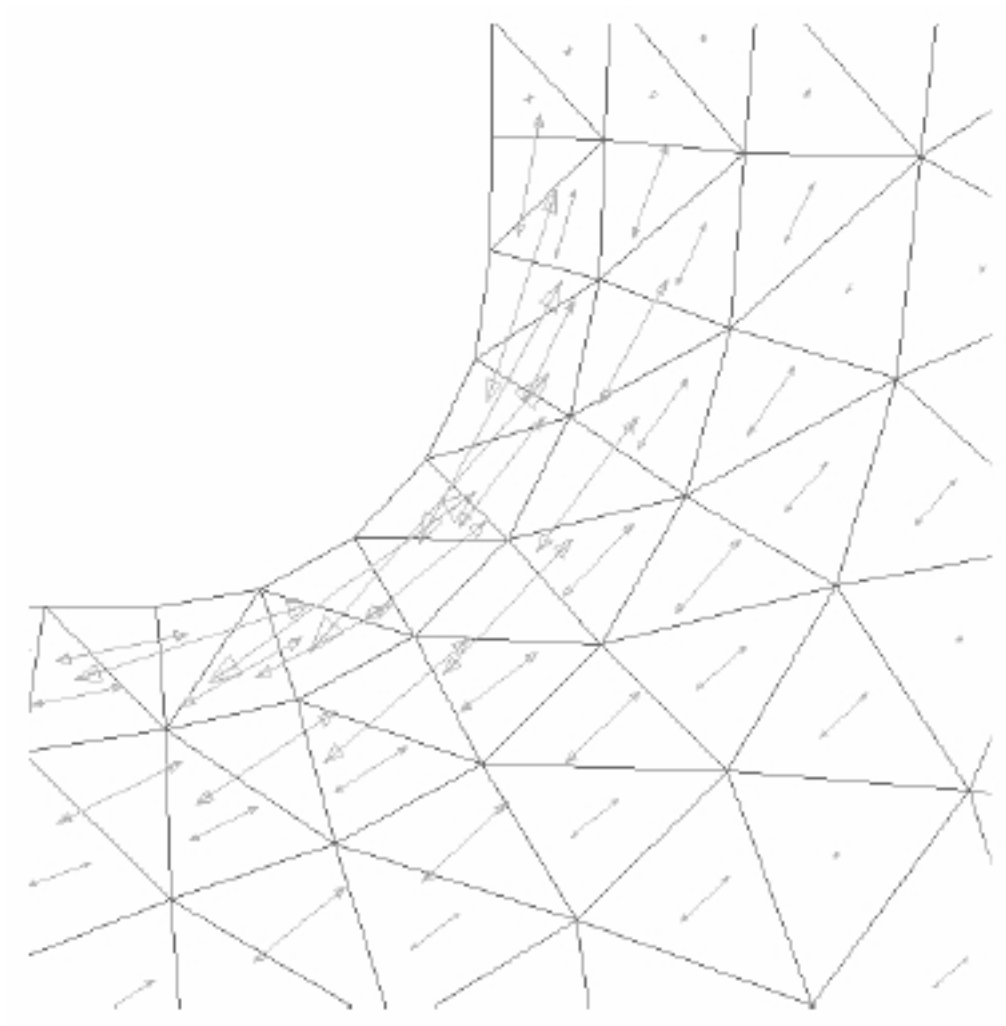


Fig. 4. Direction field of the maximum principal stress, in the rock at the bottom of the hole.

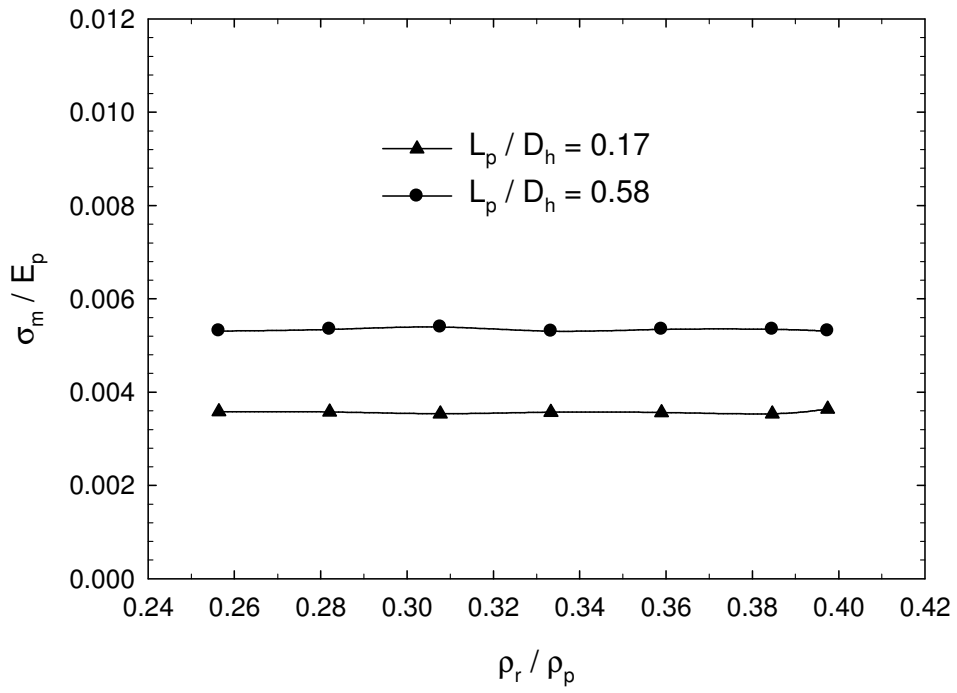


Fig. 5(a)

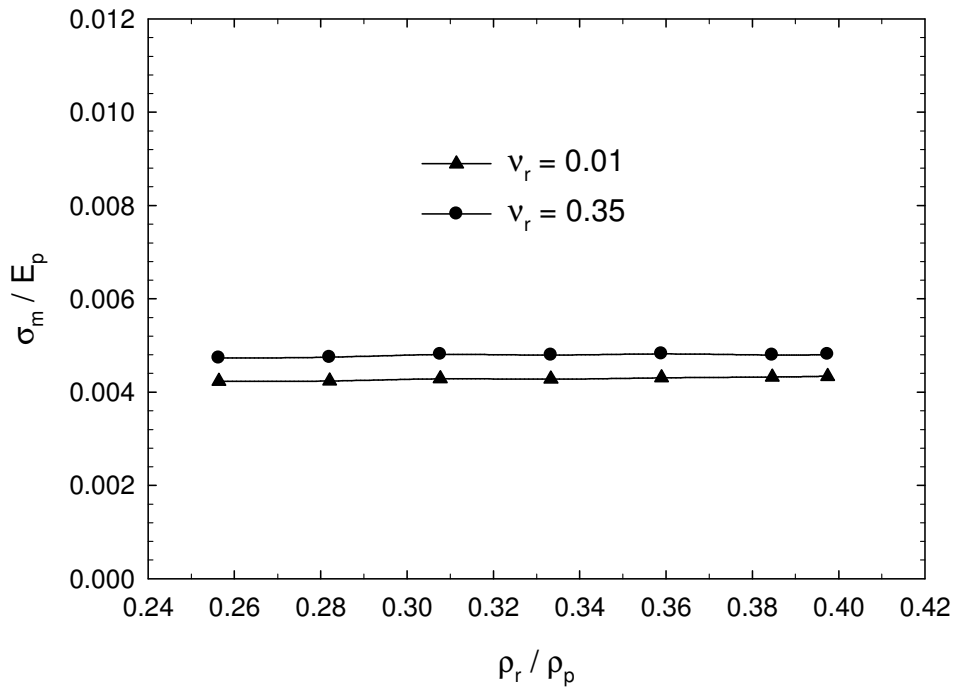


Fig. 5(b)

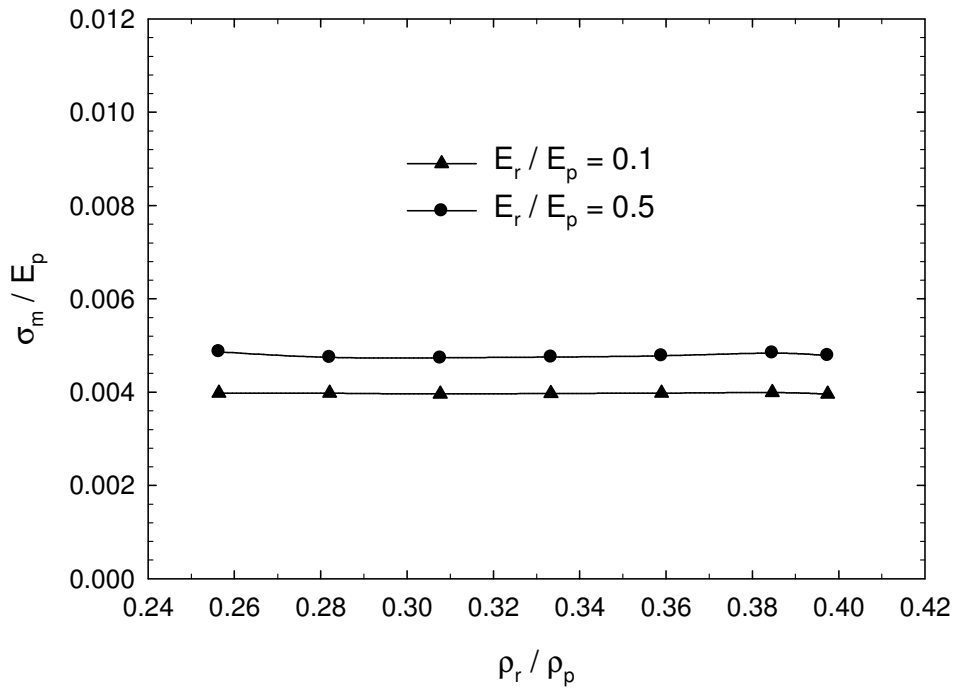


Fig. 5(c)

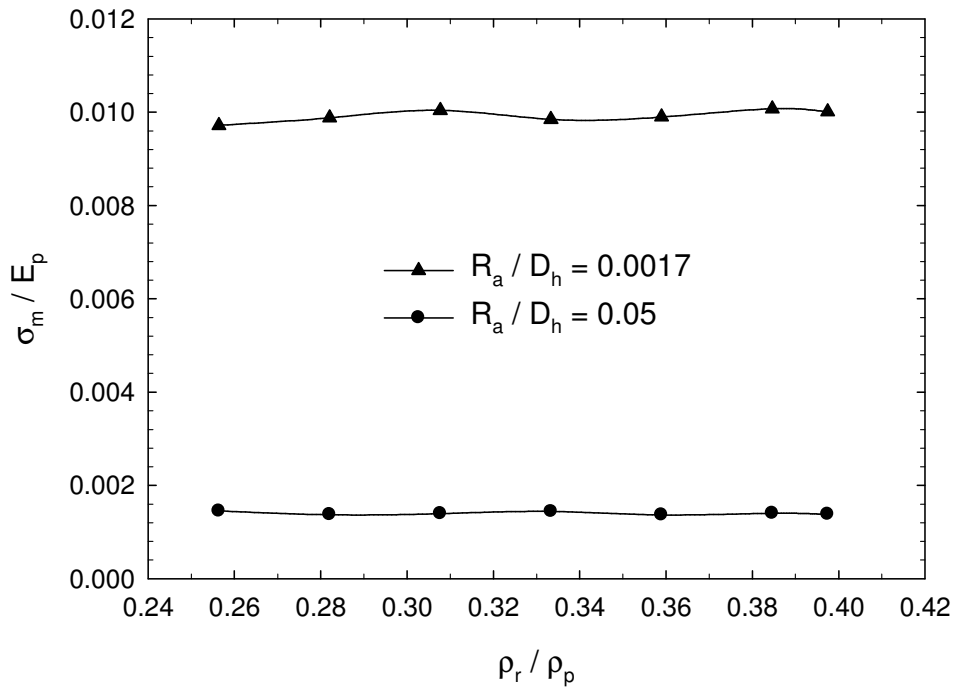


Fig. 5(d)

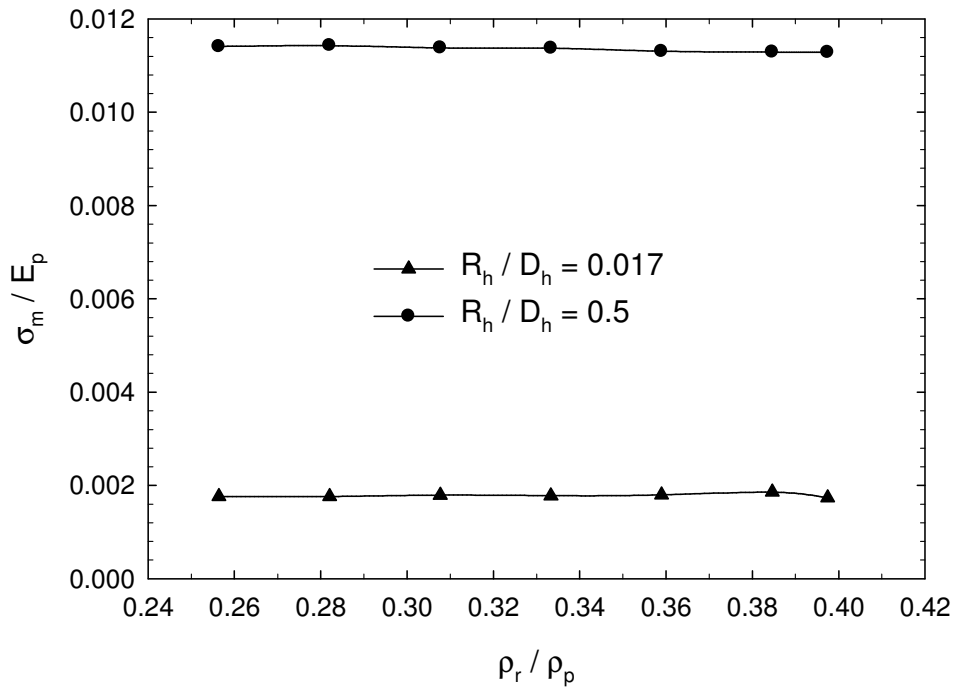


Fig. 5(e)

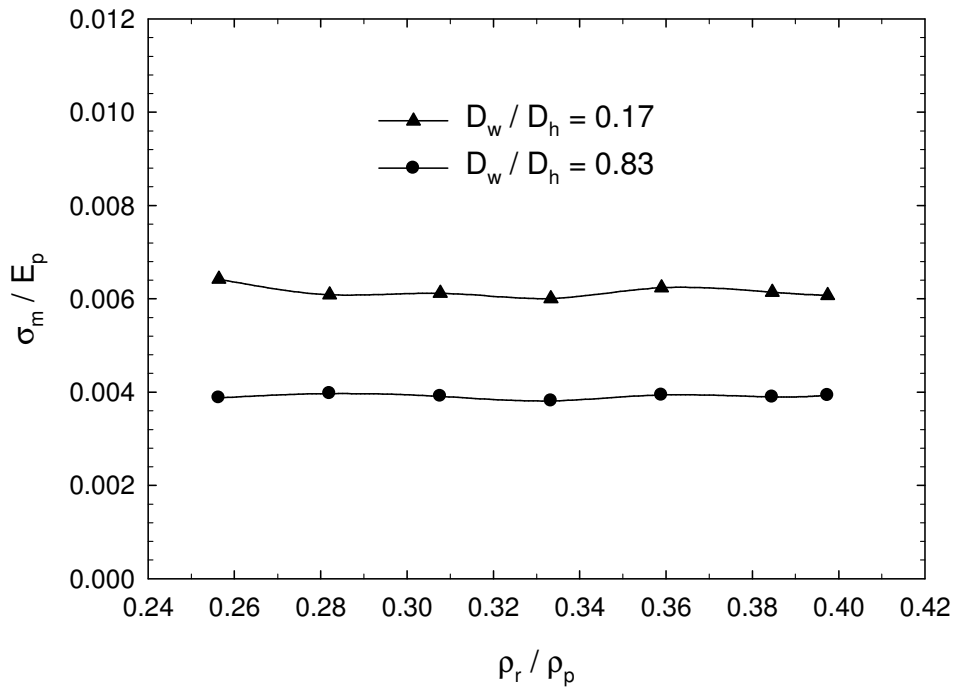


Fig. 5(f)

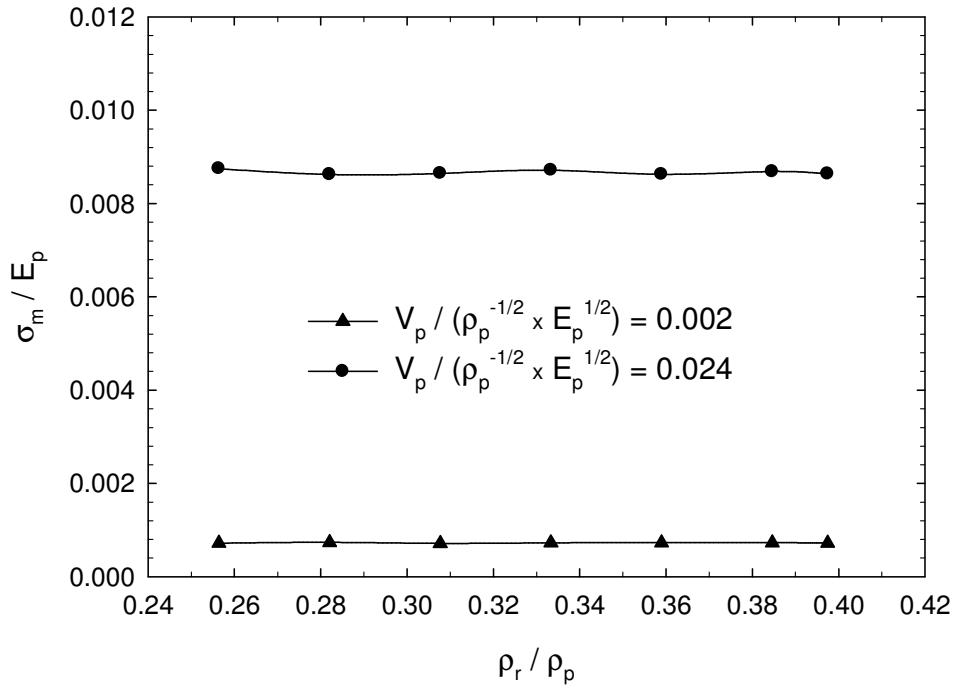


Fig. 5(g)

Fig. 5. Influence of normalized rock density on the normalized largest principal stress in the rock for the cases (a) $L_p / D_h = 0.17$ and $L_p / D_h = 0.58$; (b) $\nu_r = 0.01$ and $\nu_r = 0.35$; (c) $E_r / E_p = 0.1$ and $E_r / E_p = 0.5$; (d) $R_a / D_h = 0.0017$ and $R_a / D_h = 0.05$; (e) $R_h / D_h = 0.017$ and $R_h / D_h = 0.5$; (f) $D_w / D_h = 0.17$ and $D_w / D_h = 0.83$; (g) $V_p / (\rho_p^{-1/2} E_p^{1/2}) = 0.002$ and

$$V_p / (\rho_p^{-1/2} E_p^{1/2}) = 0.024.$$

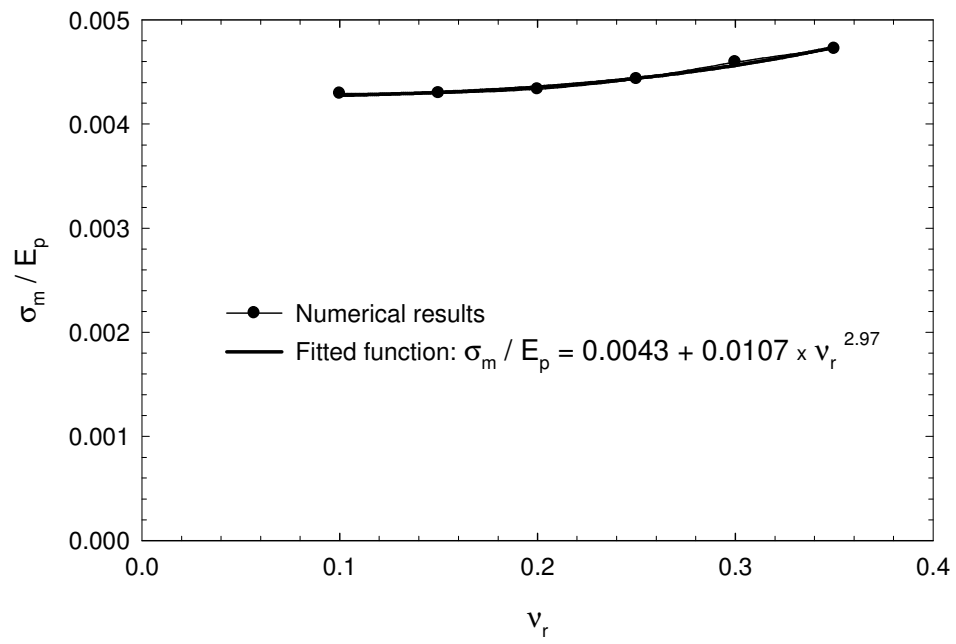


Fig. 6. Influence of Poisson's ratio of the rock on the normalized largest principal stress in the rock during the impact.

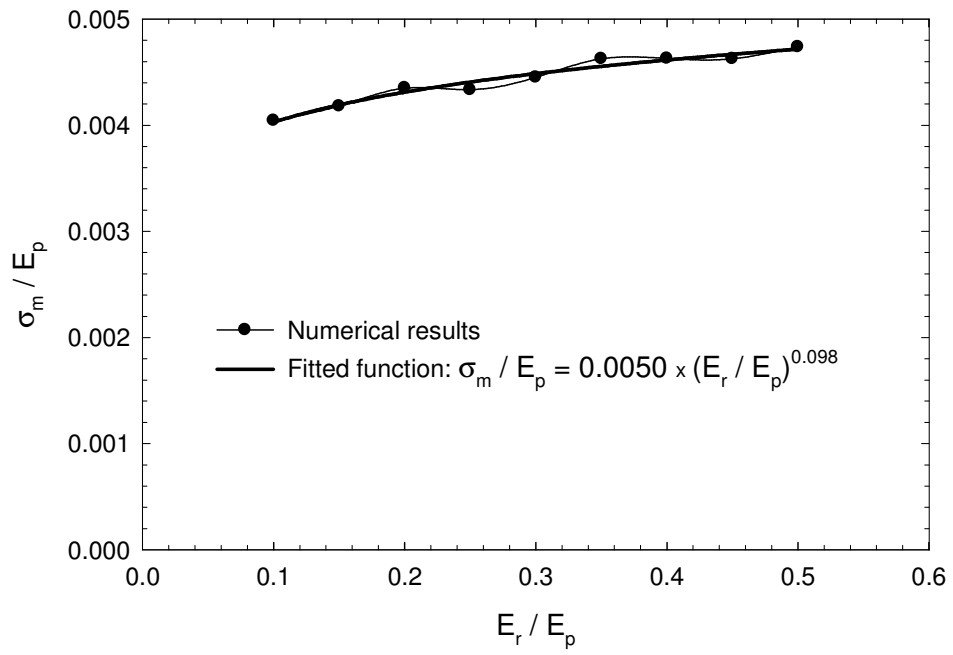


Fig. 7. Influence of normalized Young's modulus of the rock on the normalized largest principal stress in the rock during the impact.

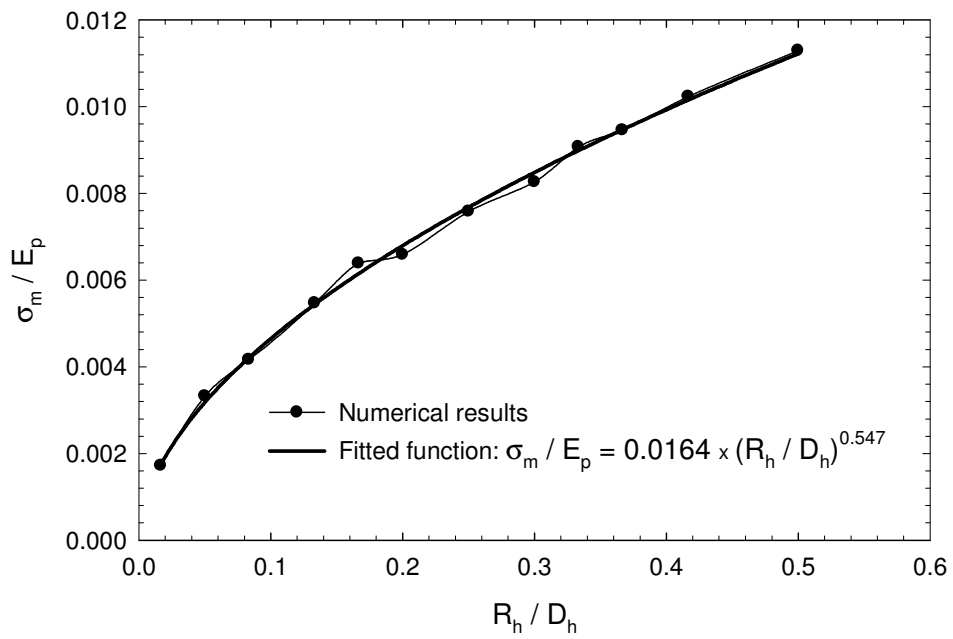


Fig. 8. Influence of normalized borehole radius on the normalized largest principal stress in the rock during the impact.

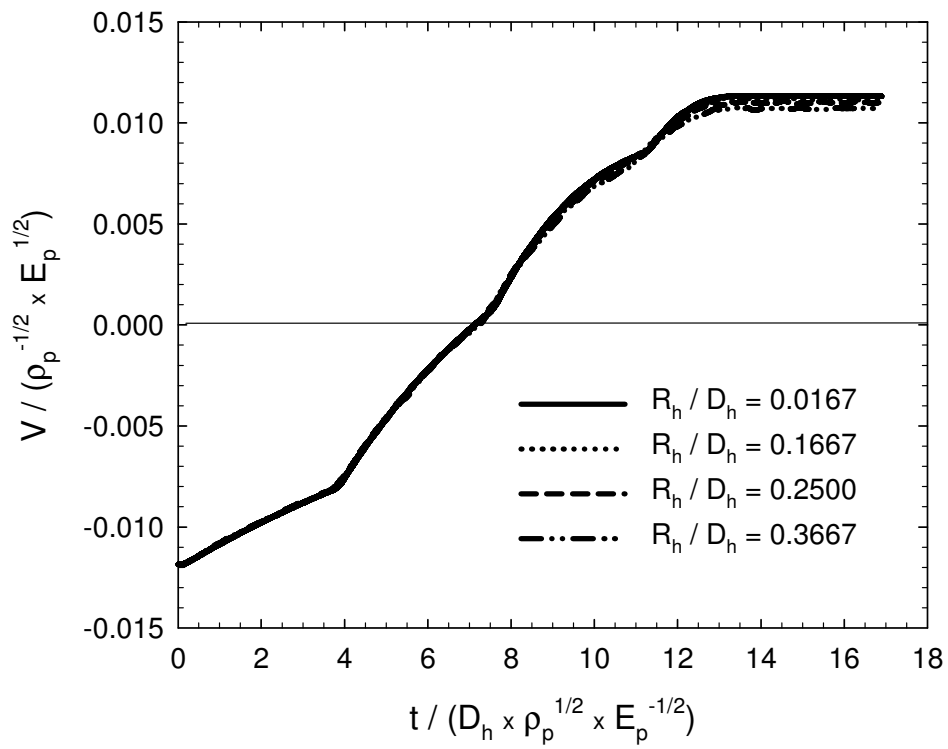


Fig. 9. Normalized average velocity of the piston versus normalized impacting time for several values of normalized borehole radius.

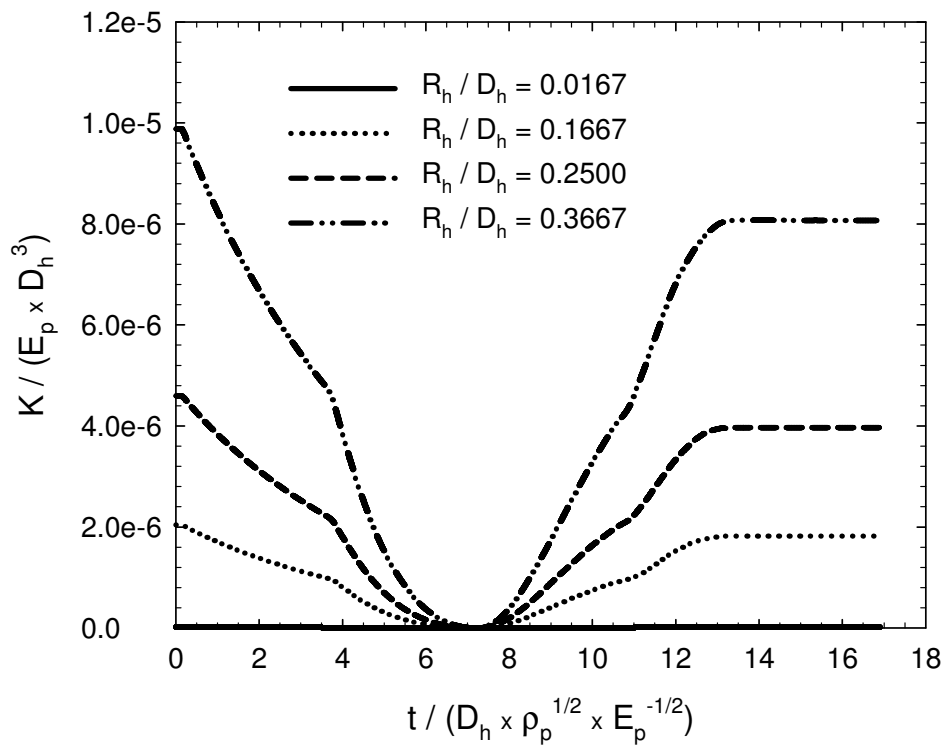


Fig. 10. Normalized kinetic energy of the piston versus normalized impacting time for several values of normalized borehole radius.

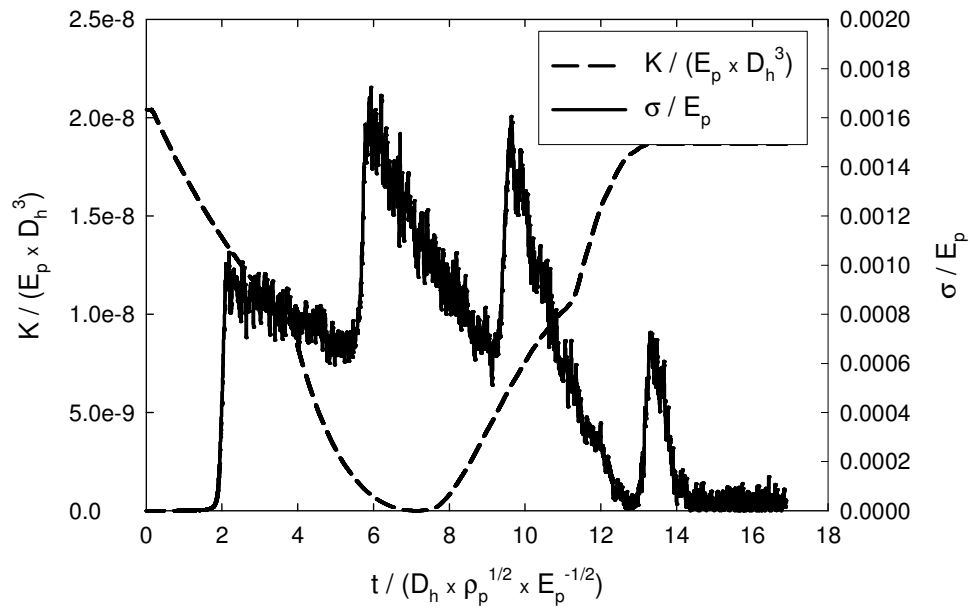


Fig. 11. Normalized energy of the piston and the normalized maximum principal stress in the element that has the largest principal stress in the rock during the impact versus normalized impacting time, for $R_h/D_h = 0.0167$.

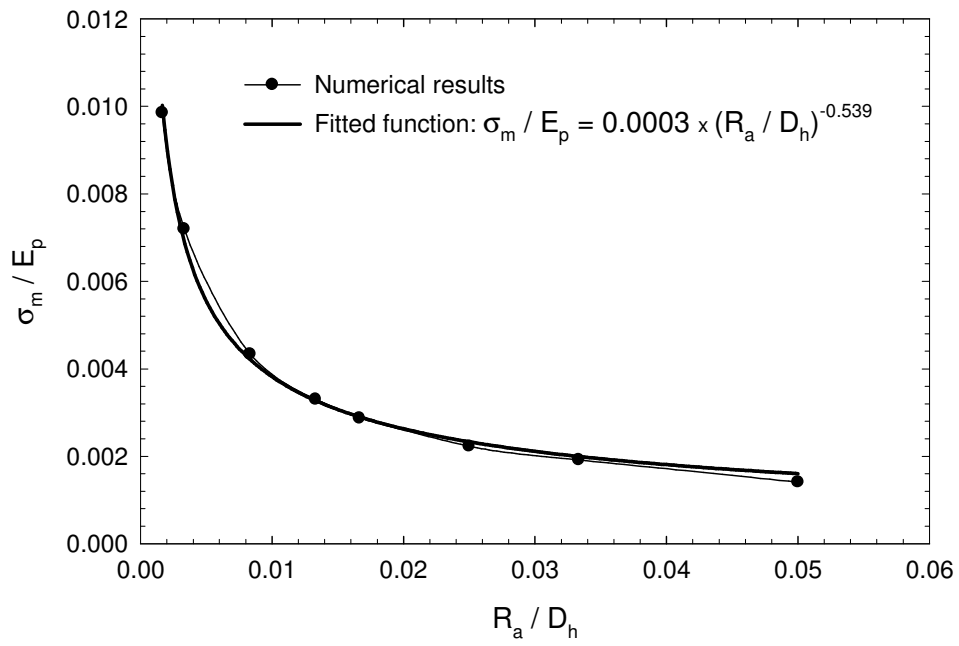


Fig. 12. Influence of normalized arc radius at the bottom of the hole on the normalized largest principal stress in the rock during the impact.

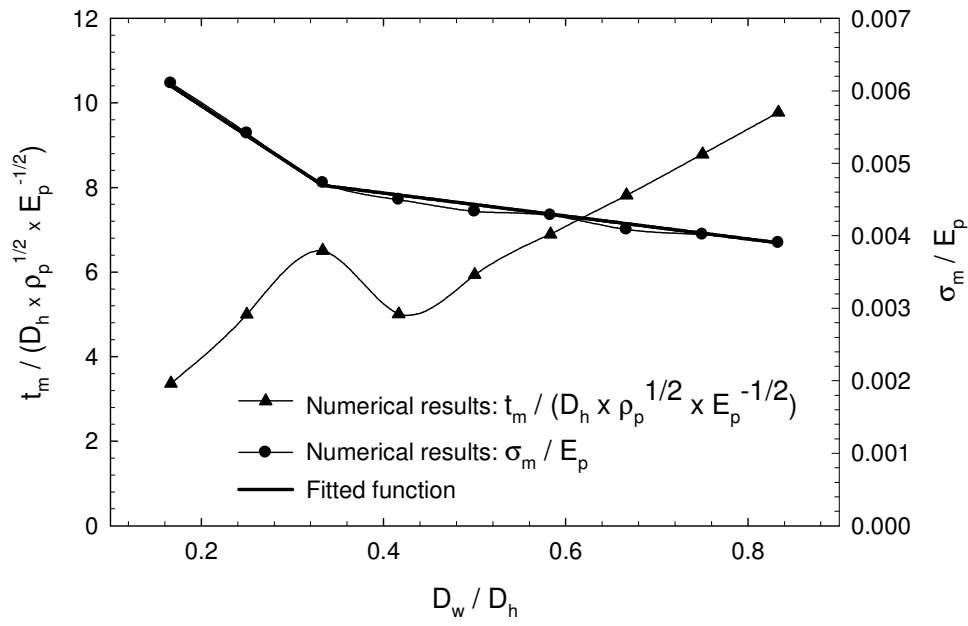


Fig. 13. Influence of normalized water depth on the normalized largest principal stress in the rock during the impact and normalized impacting time to reach that stress.

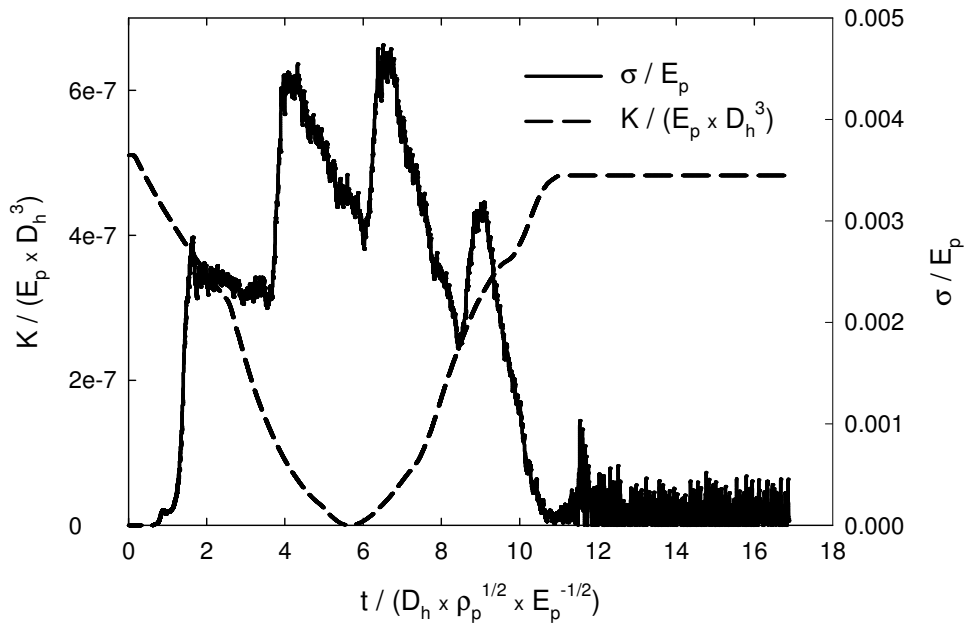


Fig. 14(a)

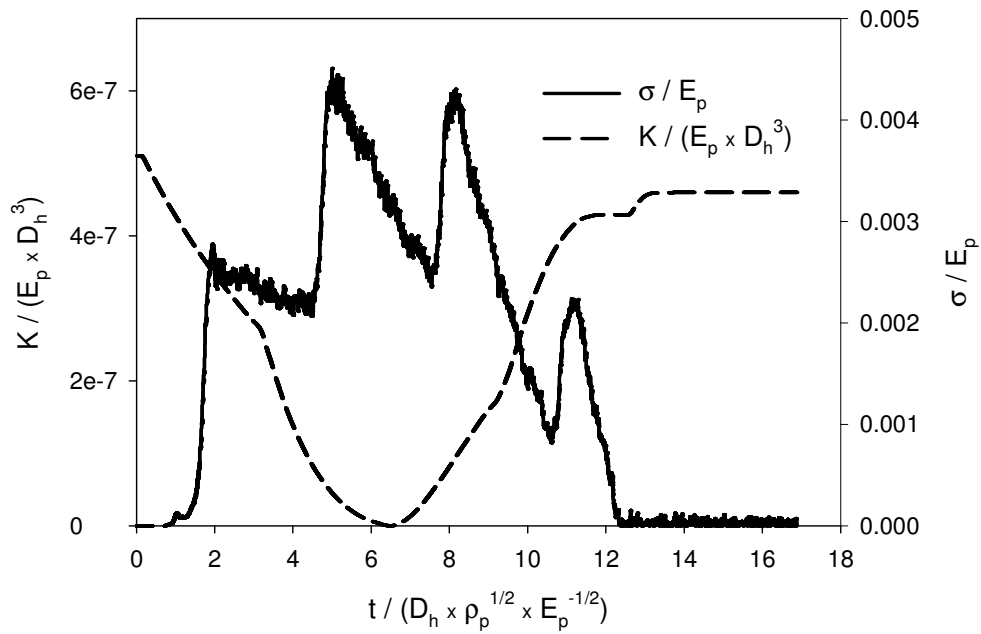


Fig. 14(b)

Fig. 14. Normalized kinetic energy of the piston and the normalized maximum principal stress in the element that has the largest principal stress in the rock during the impact versus normalized time for (a) $D_w/D_h = 0.333$ and (b) $D_w/D_h = 0.417$.

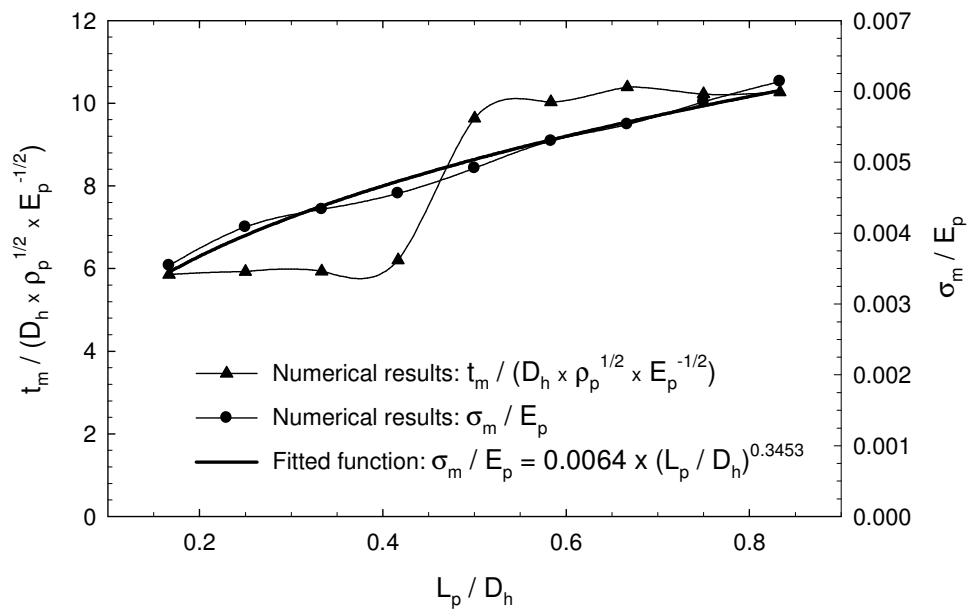


Fig. 15. Influence of normalized piston length on the normalized largest principal stress in the rock and the normalized time to reach that stress.

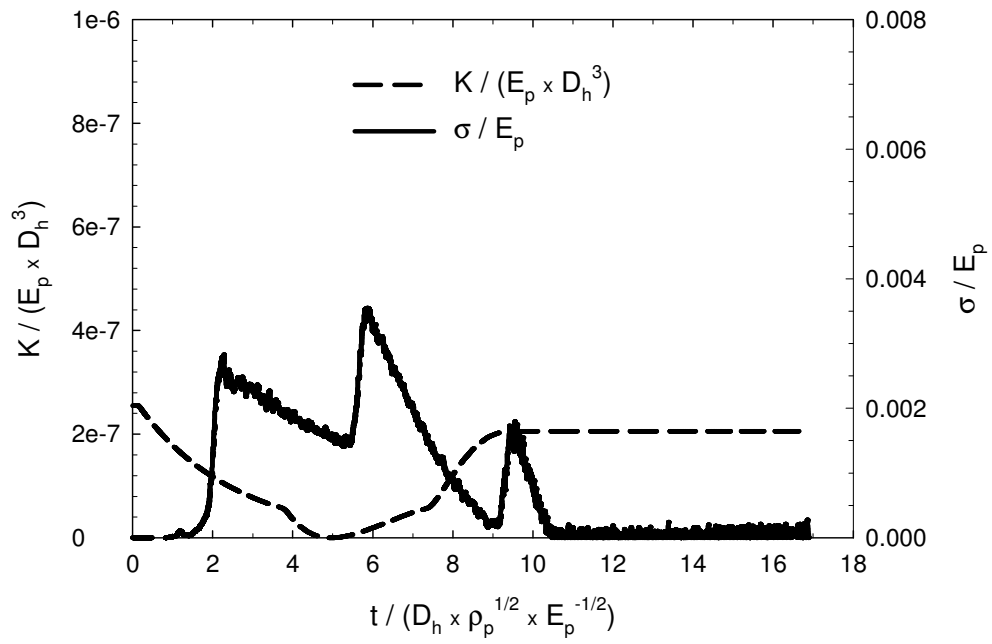


Fig. 16(a)

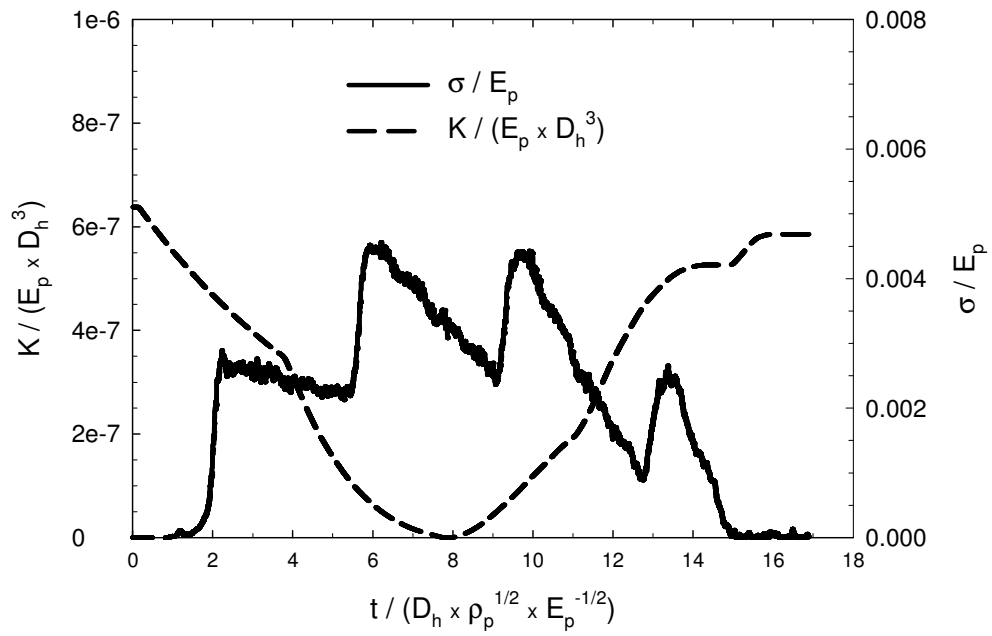


Fig. 16(b)

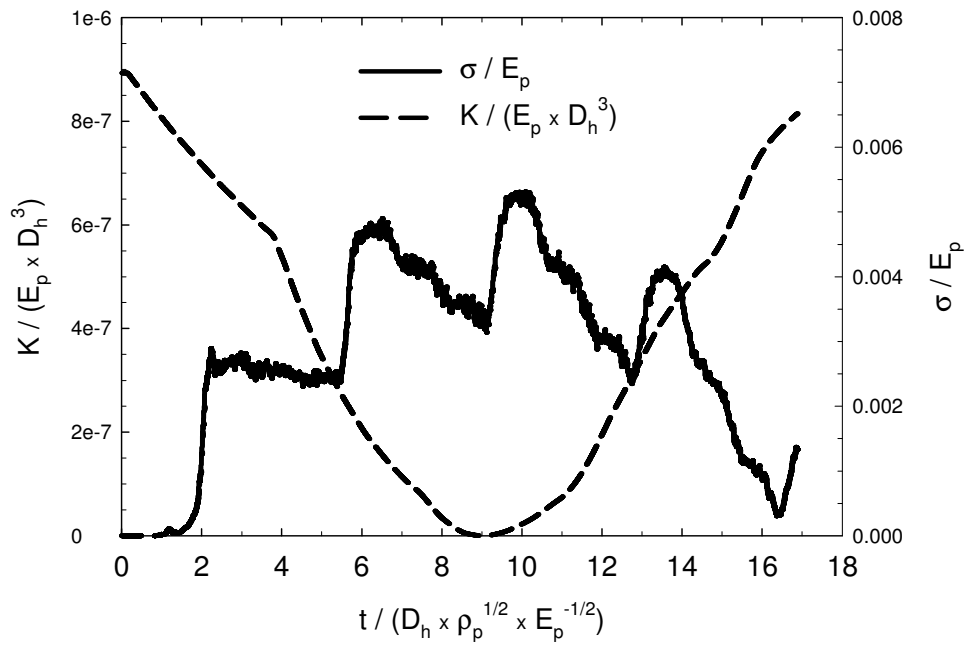


Fig. 16(c)

Fig. 16. Normalized kinetic energy of the piston and normalized first principal stress in the element that has the largest principal stress in the rock during the impact versus normalized impacting time for (a) $L_p/D_h = 0.1667$, (b) $L_p/D_h = 0.4167$ and (c) $L_p/D_h = 0.5833$.

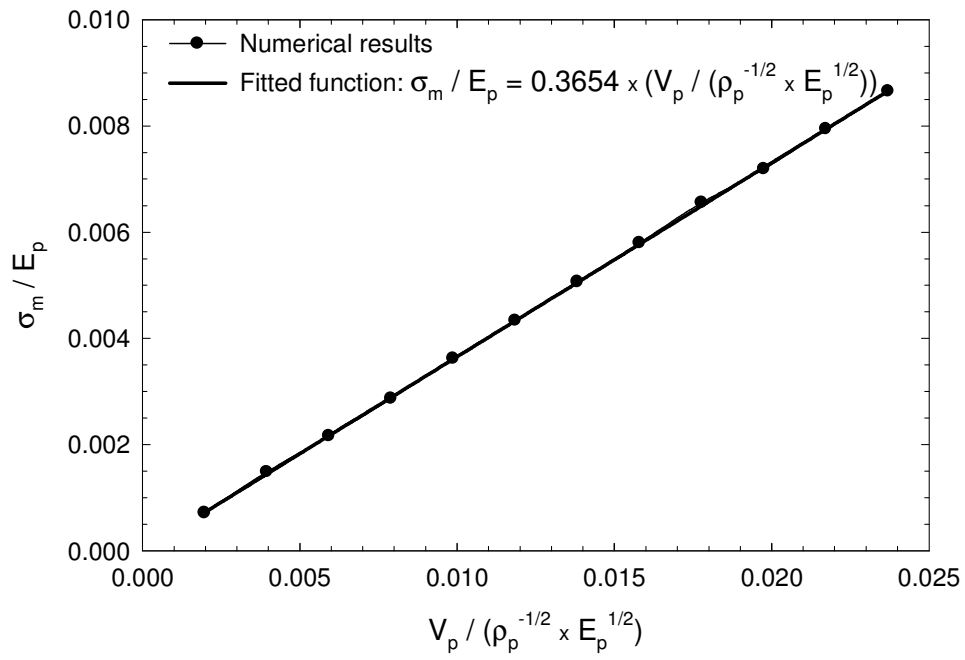


Fig. 17. Influence of normalized initial velocity of the piston on the normalized largest principal stress in the rock during the impact.

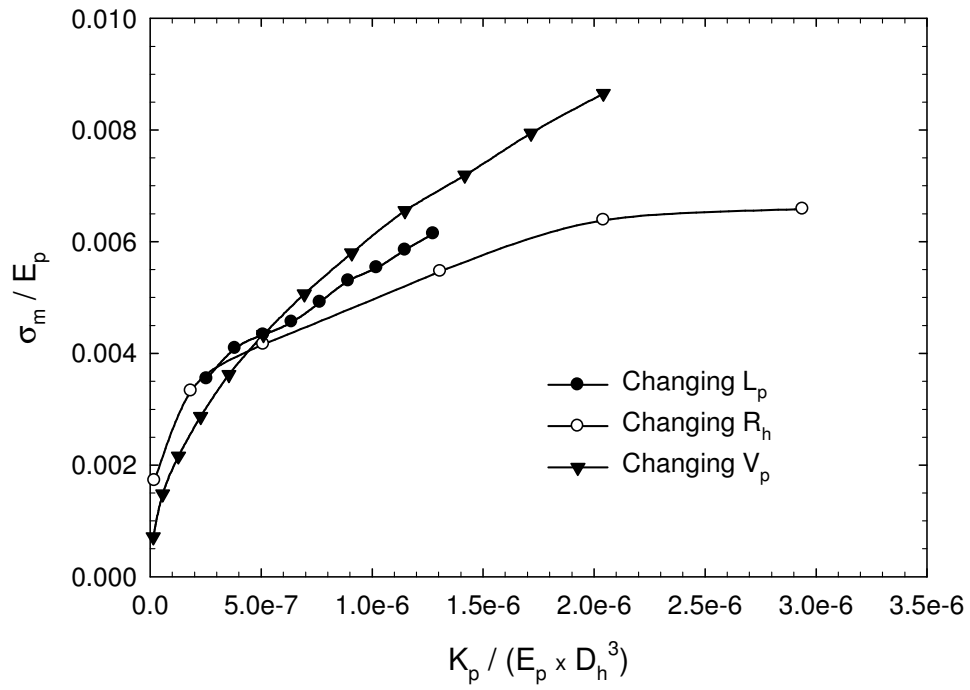


Fig. 18. Influence of normalized initial kinetic energy of the piston on normalized largest principal stress in the rock during the impact applying different ways to increase the initial kinetic energy of the piston.